

14 Introduction to Photoemission Spectroscopy

Michael Sing

Physikalisches Institut and

Röntgen Center for Complex Material Systems

Universität Würzburg

Contents

1	Introduction	2
2	The method	2
2.1	Basics	2
2.2	Many-body picture	6
3	Case studies	8
3.1	Low-energy photoemission: Doping a one-dimensional Mott insulator	8
3.2	Hard x-ray photoemission: Profiling the buried two-dimensional electron system in an oxide heterostructure	12
3.3	Resonant angle-resolved soft x-ray photoemission: Direct k -space mapping of the electronic structure in an oxide-oxide interface	14
4	Outlook	16

1 Introduction

Complex quantum materials are distinguished by their astonishingly huge variety of interesting and often peculiar electronic and magnetic properties which arise from the interplay of charge, spin, lattice, and orbital degrees of freedom. Such phenomena comprise, e.g., ferro-, pyro- and piezoelectricity, all kinds of magnetic order, colossal magnetoresistance, high-temperature superconductivity, and metal-insulator transitions. In order to arrive at a microscopic understanding of such diverse behavior the leading low-energy scales of the material under consideration have to be explored. To those, spectroscopic methods grant *direct* access by probing either low-lying single-particle or charge-neutral particle-hole and collective excitations. The former is realized, e.g., in photoelectron spectroscopy (PES) – lying at the core of this chapter – while the latter typically is implemented in scattering techniques. On the theory side, these two types of spectroscopic information correspond to the physical content of the one-particle and two-particle Green's functions, respectively. Since PES is related to the simpler one-particle Green's function and extremely versatile in that it can be applied to almost all kinds of solids it has assumed a prominent role among solid-state spectroscopies over the years, in particular whenever many-particle physics is important.

As a well established method PES is the subject of numerous monographs and review articles dealing with all kind of related aspects such as instrumentation, application to atoms, molecules, and solids, and the theoretical description [1–12]. However, it would be entirely wrong to believe that photoemission spectroscopy its theoretical understanding and implementation, is completely developed. The full calculation of photoemission spectra still represents a challenging task (cf. the chapter by J. Minar in this book) and necessitates progressively advanced methods from theory while technological evolution and innovation have made it possible, *inter alia*, to partially overcome the notorious surface sensitivity of photoemission with acceptable concessions to resolution and acquisition times.

In this chapter, after an introduction to the basics of photoemission spectroscopy the present potential of PES, in particular with regard to some modern techniques with enhanced volume sensitivity, shall be illustrated based on selected examples of complex material systems whose quantitative theoretical description often demands the advanced methods that are presented in most of the other chapters of this book. For convenience, the examples are taken from our own work.

2 The method

2.1 Basics

In a PES experiment monochromatic light is directed onto a sample. The emitted photoelectrons are discriminated with respect to their kinetic energy and, depending on the information desired, other observables like emission direction or spin, before they are detected and counted. The principle is sketched in Fig. 1, left, for an angle-resolved experiment on a single crystal.

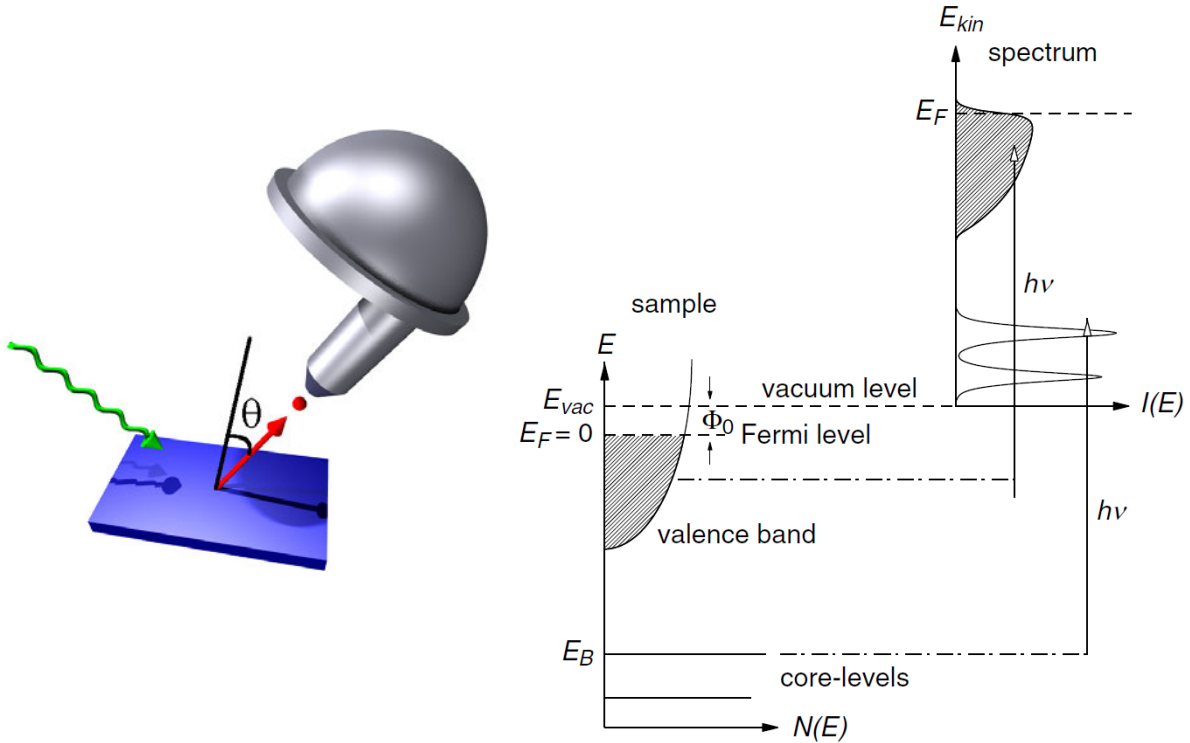


Fig. 1: *Left: Geometry for an angle-resolved photoemission experiment. Right: Energy diagram of photoemission in a one-particle picture (from [9]).*

An energy diagram of photoemission in a one-particle picture is sketched in Fig. 1, on the right. Electrons with a binding energy E_B are excited above the vacuum level E_{vac} by the absorption of a single photon with energy $h\nu$. Their kinetic energy is given by

$$E_{kin} = h\nu - E_B - \Phi_0, \quad (1)$$

where Φ_0 denotes the work function. The kinetic energy distribution of the photoelectrons in vacuum $I(E_{kin})$ then reflects essentially the occupied part of the electronic structure, i.e., the density of states in the solid (weighted by the corresponding single-particle transition matrix elements, cf. section 2.2).

If, in addition, the photoelectrons are discriminated with respect to their emission direction relative to the surface of a single-crystalline sample, the momentum \mathbf{p} is completely determined in terms of its components parallel and perpendicular to the surface. For the parallel component we have

$$\mathbf{p}_{||} = \hbar\mathbf{k}_{||} = \sqrt{2mE_{kin}} \sin \theta. \quad (2)$$

Note that $\mathbf{p}_{||}$ – due to momentum conservation – equals the parallel component of the *crystal momentum* of the electron inside the solid *in the extended zone scheme*. In contrast, due to the lack of translational symmetry perpendicular to the sample surface, the perpendicular component of crystal momentum is *not* conserved. Hence, without additional information the crystal momentum cannot be determined completely. To do so, knowledge or assumptions about the dispersion of the photoemission final states are needed (cf. Fig. 2(a)), or one resorts to advanced

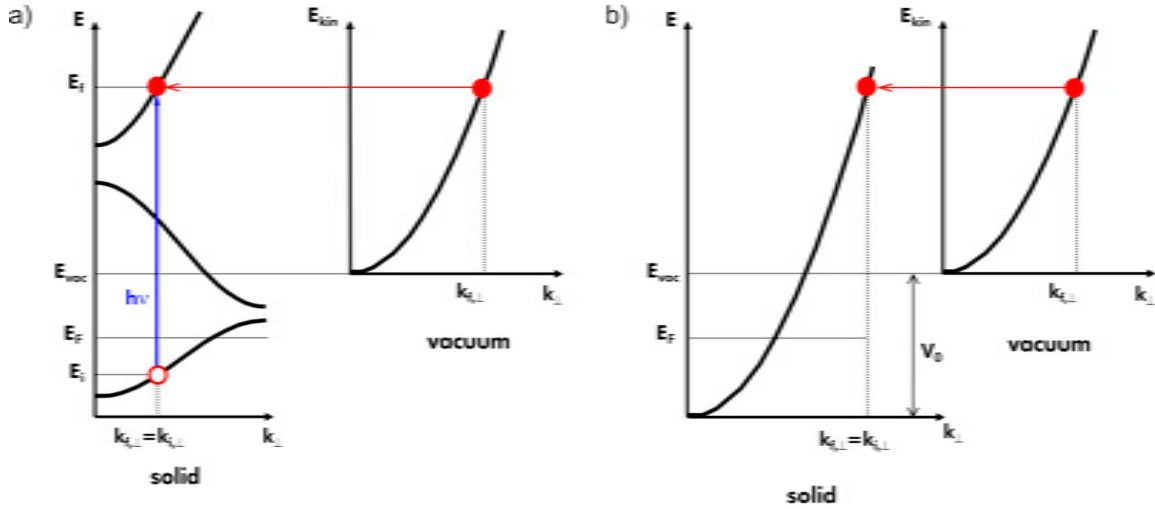


Fig. 2: Kinematics of the photoemission process. (a) Direct optical transition of an electron within the solid into a certain final state and energy of the corresponding photoelectron in vacuum. (b) Free-electron approximation for the final states in the solid and inner potential V_0 .

experimental methods which, however, are only feasible in certain cases. An often used approximation is the assumption of free electron final states. The situation is depicted in Fig. 2(b). The vertex of the parabola, describing the dispersion of the free electron final states inside the solid, is shifted along the energy axis to an energy V_0 below the vacuum level. Thus, V_0 is a measure of the depth of the potential well in a “particle-in-a-box” picture. The inner potential is a phenomenological parameter and has to be adjusted for a given material, e.g., such that the periodicity of the electron dispersions in reciprocal space with respect to k_{\perp} are reproduced for a series of PES spectra, taken in normal emission geometry (i.e., at $k_{\parallel} = 0$) at various photon energies (thereby changing k_{\perp}). Outside the solid, the reference energy for the vertex of the free-electron parabola is simply the vacuum level. With a proper choice of V_0 one can simply read off the perpendicular component of the crystal momentum as shown in Fig. 2. If one takes the inner potential into account, the equation for the perpendicular component of the crystal momentum reads

$$\mathbf{p}_{\perp} = \hbar \mathbf{k}_{\perp} = \sqrt{2m(E_{\text{kin}} \cos^2 \theta + V_0)}. \quad (3)$$

Note that for angle-integrated measurements or in the case of one- or two-dimensional systems the determination of k_{\perp} becomes irrelevant.

Using Eq. (1), Eq. (2) and, if appropriate, Eq. (3), the energy-momentum relations of electronic excitations can be inferred from the angle- or momentum-resolved energy distribution curves (EDCs) of a PES experiment by simply tracing the energy positions of marked features as is illustrated in Fig. 3(a) and (b). In the case of a non-interacting electron system these correspond to the electronic band dispersions of Bloch states (see Fig. 3(a)), in an interacting system, e.g., in a Fermi liquid, to the dispersions of quasiparticle excitations (see Fig. 3(b)). In addition, the width of the spectral features in the interacting case reflects the finite lifetime of the respective excitations and also the coupling of other degrees of freedom to the electron system which can simultaneously be excited when a photoelectron is kicked off. This is illustrated in Fig. 3(c) for

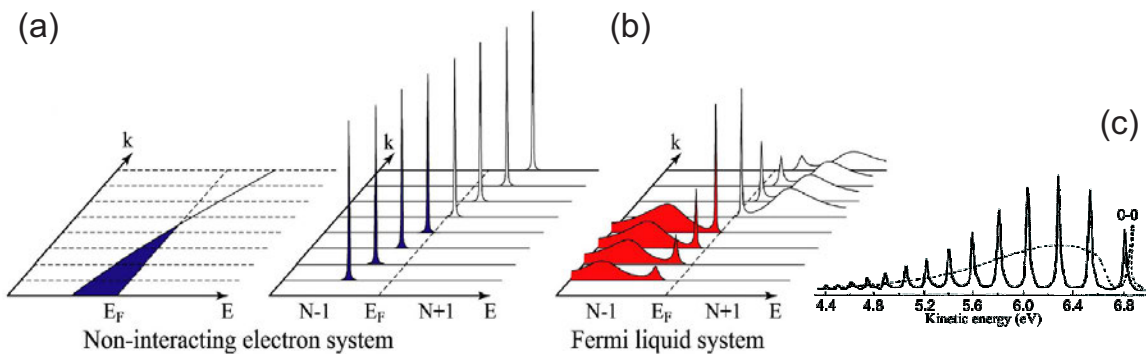


Fig. 3: Angle-resolved photoelectron spectroscopy: (a) Momentum-resolved energy distribution curves for a non-interacting electron system with a single band, crossing the Fermi energy E_F . (b) Same situation but for an interacting Fermi liquid (figure adapted from Ref. [8]) together with (c) the PES spectrum of hydrogen in the gas phase and the hypothetical spectrum for solid hydrogen (dashed line, figure adapted from Ref. [13]).

the PES spectrum of gaseous hydrogen. By kicking off a photoelectron, oscillations of the H_2 molecule are excited at the same time. Hence, besides the sharp line at about 6.8 eV as expected for the excitation from the groundstate of the rigid molecule a series of satellite lines are seen which correspond to excited vibrational states. If this spectrum is broadened, one arrives at a hypothetical spectrum (dashed line) which may serve as a paradigm of a PES spectrum for an interacting solid. It consists of a sharp, coherent quasiparticle excitation and a broad, incoherent contribution, representing the interaction of the kicked out electron with all possible excitations of the system such as phonons, magnons, spin-fluctuations, electron-hole pairs, etc.

To study the valence band of solids in the lab, usually gas discharge lamps are used whose line spectra cover the spectral range of about 10–50 eV ((AR)UPS – (angle-resolved) ultraviolet photoelectron spectroscopy). In this energy range the inelastic mean free path (IMFP) of electrons in solids, λ_{INFP} , amounts – due to the large cross section regarding plasmon excitations – only to a few Ångströms. For this reason, PES is extremely surface-sensitive.

For larger energies (>50 eV) for all materials the inelastic mean free path roughly behaves as $\lambda_{\text{INFP}} \propto \sqrt{E}$. Hence, the information depth of PES can be significantly enhanced if excitation energies in the soft ($\lambda_{\text{INFP}} \sim 15$ Å) or hard x-ray regime ($\lambda_{\text{INFP}} \sim 40$ – 100 Å) are used.¹ However, the trade-off is a strong decrease of the photoemission signal since the photoionisation cross sections within the dipole approximation scale roughly like E^{-3} . Nevertheless, during the last years high-resolution PES with soft (SXPES – soft x-ray photoelectron spectroscopy) and hard x-rays (HAXPES – hard x-ray photoelectron spectroscopy) became feasible at third generation synchrotrons. Some of the case studies presented in the following rely on the use of high photon energies beyond the standard range. If appropriate, special variants of the application of PES like resonant PES will be discussed in the respective context.

¹An enhancement of the information depth can also be achieved for excitation energies <10 eV. In this regime the IMFP is determined mainly by interband transitions which are strongly material-dependent. Hence, an increase of the information depth is not universal for this energy range.

2.2 Many-body picture

The simplest starting point for a theoretical description of photoemission is Fermi's Golden Rule. The photocurrent I results from the photoexcitation (with energy $h\nu$), described by the appropriate perturbation operator (\mathcal{H}_{int}), of the N particle system in its ground state $|\Phi_0(N)\rangle$ into all possible final states $|\Phi_{\kappa,n}(N)\rangle$. The final states also describe a system with N particles, one of them being the photoelectron with momentum $\hbar\boldsymbol{\kappa}$ and energy $(\hbar\boldsymbol{\kappa})^2/2m$. The index n denotes a complete set of quantum numbers defining all possible excitations in the final state. Hence the expression of the photocurrent is given by

$$I_{\kappa}(h\nu) = \frac{2\pi}{\hbar} \sum_n |\langle \Phi_{\kappa,n}(N) | \mathcal{H}_{\text{int}} | \Phi_0(N) \rangle|^2 \delta(E_{\kappa,n}(N) - E_0(N) - h\nu). \quad (4)$$

The operator \mathcal{H}_{int} describes the interaction of the photon field with a single electron within first-order perturbation theory. In second quantization it reads

$$\mathcal{H}_{\text{int}} = \sum_{i,j} \langle \mathbf{k}_i | \mathcal{H}_{\text{int}} | \mathbf{k}_j \rangle c_i^\dagger c_j = \sum_{i,j} M_{ij} c_i^\dagger c_j. \quad (5)$$

In the corresponding description based on the Schrödinger equation the explicit representation of \mathcal{H}_{int} is obtained by the canonical replacement of momentum according to $\mathbf{p} \rightarrow \mathbf{p} - e\mathbf{A}$, where \mathbf{A} is the vector potential of the photon field

$$\mathcal{H}_{\text{int}} = -\frac{e}{2m} (\mathbf{A} \cdot \mathbf{p} + \mathbf{p} \cdot \mathbf{A}) + \frac{e^2}{2m} \mathbf{A}^2. \quad (6)$$

The term quadratic in \mathbf{A} is only important in the case of very high photon intensities and can usually be neglected even when employing highly brilliant synchrotron radiation. Using the commutator relation $[\mathbf{p}, \mathbf{A}] = -i\hbar\nabla\mathbf{A}$ and under the assumption $\nabla\mathbf{A} \approx 0$, which corresponds to the dipole approximation valid for typical photon energies in the vacuum ultraviolet,² the perturbation operator can be simplified further, yielding

$$\mathcal{H}_{\text{int}} = -\frac{e}{m} \mathbf{A} \cdot \mathbf{p}. \quad (7)$$

The matrix element in Eq. (4) can be further evaluated in the case of a factorized final state. It then can be written as a product of the state of the photoelectron and the state of the remaining $(N - 1)$ particle system

$$|\Phi_{\kappa,n}(N)\rangle = c_{\kappa}^\dagger |\Phi_n(N - 1)\rangle. \quad (8)$$

This approximation, known as *sudden approximation* is all but trivial. From a physical point of view, it means that the photoelectron is removed instantaneously, i.e., relaxation processes during photoemission are neglected. In general, it is assumed that this assumption is well justified for photon energies of several tens of eV and beyond [14]. From Eq. (4) with Eq. (5) one gets

$$I_{\kappa}(h\nu) = \frac{2\pi}{\hbar} \sum_j |M_{\kappa j}|^2 \sum_n |\langle \Phi_n(N - 1) | c_j | \Phi_0(N) \rangle|^2 \delta(\varepsilon_{\kappa} + E_n(N - 1) - E_0(N) - h\nu). \quad (9)$$

²At surfaces, due to the discontinuity of the dielectric function, this assumption is not necessarily fulfilled, which can lead to special surface effects.

Introducing the chemical potential, $\mu = E_0(N) - E_0(N - 1)$, and with $\varepsilon = \varepsilon_{\kappa} - h\nu - \mu$ (i.e., energies are negative with respect to the chemical potential) the final expression for the photocurrent reads

$$\begin{aligned} I_{\kappa}(h\nu) &= \frac{2\pi}{\hbar} \sum_j |M_{\kappa j}|^2 \sum_n |\langle \Phi_n(N-1) | c_j | \Phi_0(N) \rangle|^2 \delta(\varepsilon + E_n(N-1) - E_0(N-1)) \\ &= \frac{2\pi}{\hbar} \sum_j |M_{\kappa j}|^2 A^<(\mathbf{k}_j, \varepsilon), \end{aligned} \quad (10)$$

where $A^<(\mathbf{k}_j, \varepsilon)$ is the electron removal spectral function at $T = 0$. Under the assumption that the one-particle matrix elements $M_{\kappa j}$ conserve momentum and are constant, angle-resolved photoemission thus essentially measures the momentum-resolved spectral function $A^<(\kappa, \varepsilon)$. The spectral function has a simple and instructive interpretation in terms of a quantum mechanical measurement. Kicking out an electron from the groundstate prepares the system in an excited $(N - 1)$ particle state. This hole state, in general, is not an eigenstate of the $(N - 1)$ particle system. Hence, when predicting the result of an energy measurement in photoemission this state has to be projected onto the eigenstates $|\Phi_0(N - 1)\rangle$. Their relative contribution to the prepared hole state is then sampled in a PES experiment. The δ function simply ensures energy conservation.

In other words, the spectral function describes the probability to remove an electron from the system with wavevector \mathbf{k} and energy ε . In the case of independent electrons $c_j|\Phi_0(N)\rangle$ in Eq. (10) is exactly an eigenstate of the $(N - 1)$ particle system, and $A^<(\mathbf{k}, \varepsilon)$ becomes a δ function. Integration over \mathbf{k} yields the one-particle density of states. For integration over ε the sum rule $\int_{-\infty}^{\infty} d\varepsilon A(\mathbf{k}, \varepsilon) = 1$ applies, when the spectral function is generalized also to the case that a particle is added to the system.

For a theoretical treatment the spectral function is in most cases only of limited use since a direct calculation in principle requires the knowledge of all excited states of the $(N - 1)$ particle system. The major role of photoemission for the investigation of interacting electron systems stems from the fact that the spectral function is simply related to the already mentioned one-particle Green's function $G(\mathbf{k}, \varepsilon)$, for the calculation of which there exist many powerful methods. The relation is

$$A^<(\mathbf{k}, \varepsilon) = -\frac{1}{\pi} \text{Im} G(\mathbf{k}, \varepsilon - i0^+) f(\varepsilon, T), \quad (11)$$

where $f(\varepsilon, T)$ is the Fermi-Dirac distribution.

The Green's function that contains the full dynamics of an interacting many-particle system can be expressed in terms of the single-particle energy $\varepsilon_{\mathbf{k}}^0$ and a complex self-energy $\Sigma(\mathbf{k}, \varepsilon) = \Sigma'(\mathbf{k}, \varepsilon) + i\Sigma''(\mathbf{k}, \varepsilon)$

$$G(\mathbf{k}, \varepsilon) = \frac{1}{\varepsilon - \varepsilon_{\mathbf{k}}^0 - \Sigma(\mathbf{k}, \varepsilon)}. \quad (12)$$

The self-energy contains all interaction and correlation effects. With the self-energy Eq. (11) can be rewritten as

$$A(\mathbf{k}, \varepsilon) = -\frac{1}{\pi} \frac{\Sigma''(\mathbf{k}, \varepsilon)}{[\varepsilon - \varepsilon_{\mathbf{k}}^0 - \Sigma'(\mathbf{k}, \varepsilon)]^2 + [\Sigma''(\mathbf{k}, \varepsilon)]^2}, \quad (13)$$

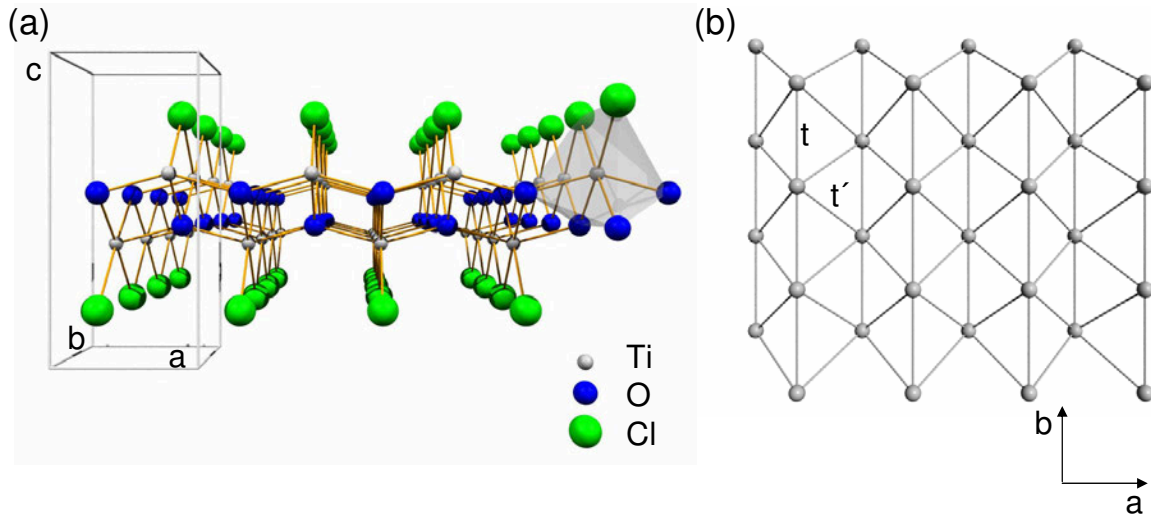


Fig. 4: (a) Crystal structure of TiOCl along the b -axis. Ti-O bilayers, sandwiched by chlorine ions, are stacked along the c -axis with sizable van der Waals gaps in between. (b) Triangular-type lattice of the Ti ions viewed along the c -axis (from [10]).

which again has a simple interpretation. For fixed ε and with $\Sigma''(\mathbf{k}, \varepsilon)$ only weakly varying with \mathbf{k} , Eq. (13) represents a Lorentzian whose finite width is determined by $\Sigma''(\mathbf{k}, \varepsilon)$ and whose renormalized energy position is given by $\Sigma'(\mathbf{k}, \varepsilon)$. Hence, the full information about the finite lifetime of the excitations and the renormalization of the electronic dispersions due to interactions as contained in the self-energy can be determined experimentally from an analysis of ARPES spectra.

While the above expression for the photocurrent in Eq. (10) is general, one should be aware of the fact that it is usually evaluated using *bulk* Bloch states, thereby neglecting the existence of a surface and the concomitant special nature of the states in a real PES experiment. To heal this shortcoming, the resulting spectral function is considered only the first step in a so-called three-step-model in which the photoemission process is described by the initial optical excitation in the solid, the propagation of the photoelectron to the surface including scattering events, and the transmission into the vacuum across the surface potential barrier. A proper treatment of photoemission as a one-step process clearly is much more challenging to theory (cf. J. Minar's contribution in this book).

3 Case studies

3.1 Low-energy photoemission: Doping a one-dimensional Mott insulator

In the nineties, TiOCl was discussed as a material in which a resonating valence bond state, if driven metallic, might result in exotic superconductivity [15]. Indeed, more recent results reported on an unusual spin-Peierls scenario due to the geometric frustration of magnetic interactions and a spin dimerized ground state [16–18], thus reviving the idea of superconductivity induced by some kind of bond-dimer fluctuations if it is possible to introduce additional charge carriers into the system.

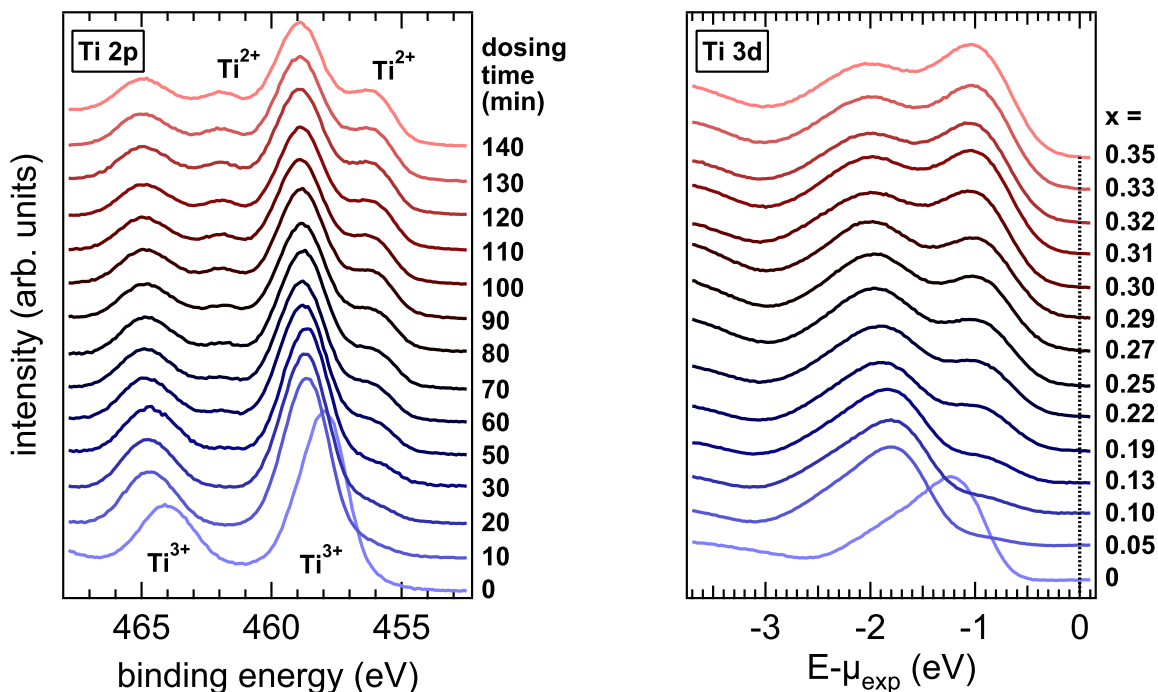


Fig. 5: Left: Ti 2p spectra of TiOCl after various durations of Na dosing. Right: Corresponding Ti 3d spectra. The electron doping concentration x can be inferred from the Ti 2p spectra (from [20]).

The structure of TiOCl is depicted in Fig. 4. It is a layered material [19] with one-dimensional Ti chains running along the crystallographic b -axis (see Fig. 4). Also note that the Ti sites, if projected onto the (a, b) -plane, form a triangular lattice giving rise to the geometric frustration of magnetic interactions which, however, is weak since the hopping amplitudes along and across the chains differ by one order of magnitude.

Beside the interest in this compound as a spin- $1/2$ quantum magnet with unusual properties and the perspective of exotic superconductivity, TiOCl deserves also attention since at room temperature it is a clean realization of a quasi-one-dimensional Mott insulator with the Ti ions in a $3d^1$ configuration and the orbital degrees of freedom quenched (the occupied d_{xy} orbital is slightly split off from the next higher $d_{yz, zx}$ orbitals).

One way of doping the system is by intercalation of alkali metal atoms into the layered structure. This can be achieved *in situ* by the evaporation of alkali metal atoms onto the surface of a freshly cleaved crystal. That the occupancy of the d shell can indeed be enhanced in this way is shown in the left panel of Fig. 5, which shows XPS spectra of the Ti 2p core level [20]. With increasing duration of Na dosing, additional spectral weight appears at lower binding energies with respect to the two main lines. This can be attributed to the emission from the 2p shell of Ti ions that are in a 2+ instead of a 3+ oxidation state. The extra electron in the valence shell leads to a more effective screening of the core potential and hence to a shift of the core levels to lower binding energies (so-called chemical shift). From an analysis of the areas of the respective Ti 2p lines the amount of electron doping into the Ti 3d states can be determined quite accurately according to $x = A(2+)/ (A(2+) + A(3+))$.

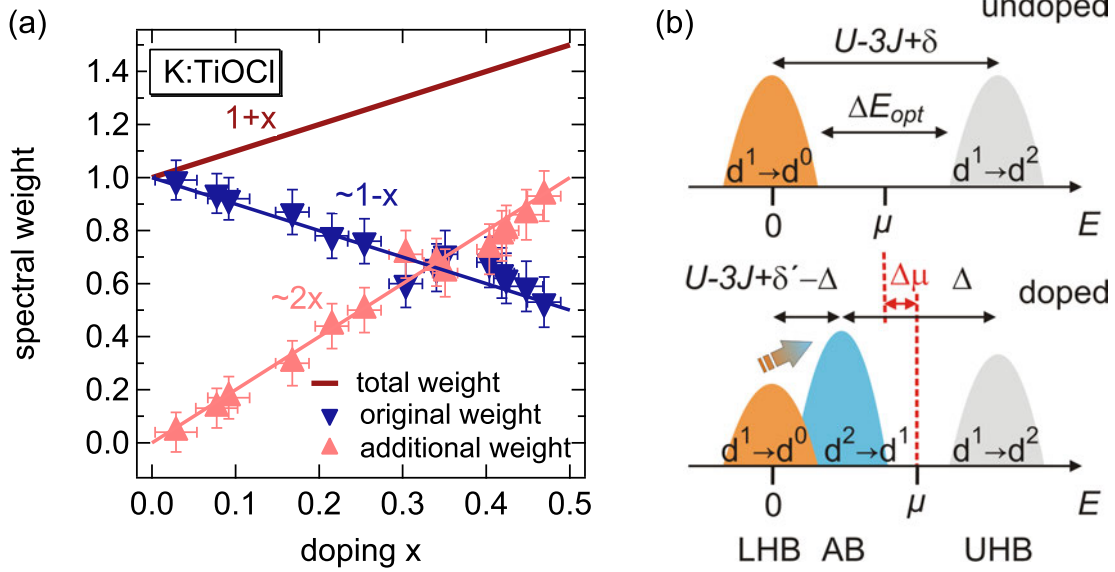


Fig. 6: (a) Quantitative analysis of the transfer of Ti 3d spectral weight upon doping. (b) Sketch of the spectral function of TiOCl for the undoped and doped case. The arrow indicates the transfer of spectral weight (from [20]).

The change in the Ti 3d weight at the chemical potential upon electron doping can be seen in the angle-integrated PES spectra of the right panel of Fig. 5 [20]. For $x = 0$ only the lower Hubbard band (LHB) and a clear gap is seen. Already for the lowest doping level the whole spectrum is shifted by about 0.6 eV to higher binding energies. With increasing x additional spectral weight develops near the chemical potential which overlaps with the lower Hubbard band. Surprisingly, no metallic phase, which would be signalled by a sharp quasiparticle peak at the chemical potential, is observed for any doping level as one would expect in a Mott Hubbard scenario. If the initial shift of the spectrum was interpreted as jump of the chemical potential from the middle of the Mott gap to the lower edge of the upper Hubbard band (UHB) it should amount to about half the optical gap of about 2 eV. However, it is significantly smaller. Further, upon closer inspection it is recognized that the spectral weight of the LHB decreases in favor of the additional weight upon doping.

A quantitative analysis of the data as shown in Fig. 6(a) – here for the case of K intercalation – reveals the following relationship: If the total Ti 3d weight, for which a sum rule applies (cf. section 2.2), is normalized to $1 + x$ and the integral intensities of both components are plotted as a function of doping x , it is seen that the LHB weight decreases as $1 - x$, while the additional weight upon doping increases as $2x$ [20]. This so-called transfer of spectral weight is exactly what is expected in the atomic limit ($t = 0$), i.e., when there is no quasiparticle, for the lower and upper Hubbard bands of a Mott insulator. For each extra electron on a Ti site there is one possibility lost to remove by PES an electron at the orbital energy ε while there are now two possibilities to take out an electron from a doubly occupied site at the single particle energy $\varepsilon + U$. Thus it is spectroscopically proven that both bands are correlated, i.e., they behave as LHB and UHB.

To understand the puzzling observations that no metallic phase is induced despite significant electron doping and that the size of the jump of the chemical potential does not match half the optical gap one has to consider unwanted side effects induced by chemical intercalation apart from the addition of electrons to the $3d$ shell. The salient point is that the alkali metal ions are not randomly distributed between the layers but assume only well-defined positions close to certain Ti sites [21, 22]. The consequences are two-fold: Firstly, the outer electron of the alkali metal is donated exactly to the Ti ion situated next to it. Secondly, the now positively charged alkali metal ion induces a sizable Coulomb potential at the next Ti site leading to a shift of the Ti $3d$ orbital energies at this site towards higher binding energies. In this way, a second sort of Ti site with renormalized orbital energies is created electrostatically, a mechanism that one could call electrostatic alloying. A further consequence of this scenario is that an electron double occupancy can only occur at such alloy sites. In PES these give rise to the observed additional spectral weight, viz. the alloy band (AB) within the original Mott gap between LHB and UHB. Hence, the system remains insulating for all doping concentrations. This qualitative picture is sketched in Fig. 6(b) [20]. For each spectral structure, the transitions in terms of the local electronic configuration of the d shell upon removal of an electron as in PES are also noted. This scenario bears some resemblance to ionic or alloy Hubbard models. However, within these models doping at some stage always leads to metallic phases. The difference to the situation encountered in experiment is that in these models the potential varies in an alternating manner or statistically for a fixed number of sites. In contrast, by the very method of doping through chemical intercalation the number of alloy sites is changed dynamically.

This qualitative picture can also be corroborated quantitatively. The energy for adding a second electron to the d shell of a Ti ion amounts to $U - 3J + \delta$ since for parallel spin orientation of the electrons in two different orbitals an exchange energy $3J$ is gained [23]. Here the energy splitting of the two lowest lying orbitals is taken into account by $\delta \approx 0.3$ eV. Upon intercalation this splitting is reduced to $\delta' \approx 0.1$ eV at the alloy sites [22]. The electrostatic potential at the alloy sites due to adjacent alkali metal ions is denoted by Δ . This yields an energy separation $U - 3J + \delta' - \Delta$ of LHB and AB. Note that the energy separation of LHB and UHB remains unchanged and is given by $U - 3J + \delta$. Experimentally, it amounts to about 1 eV. The chemical potential jumps by half this value – exactly as observed in the PES spectra – assuming that it is lying in mid-gap position, now between AB and UHB. Inserting feasible values for $U - 3J$ between 2.5 and 3.5 eV [23, 24], yields $\Delta \approx 2$ eV. This value can be reconciled within a simple, local model of point charges. If for all crystallographically inequivalent Ti sites the Coulomb potential due to a single, intercalated, positively charged alkali metal ion and an extra electron residing on the Ti site next to it is calculated, taking screening into account by a dielectric constant of 3.5 [25], one obtains a value of about 2 eV for a doubly occupied Ti site while the potential for the other Ti ions remains essentially unchanged. TiOCl , if n -doped by intercalation with alkali metal ions, hence turns out to be a special case of an alloy-Mott insulator where the alloy sites are created dynamically by the dopants themselves due to electrostatics.

3.2 Hard x-ray photoemission: Profiling the buried two-dimensional electron system in an oxide heterostructure

Transition metal oxides are well-known for their huge variety of intrinsic functionalities such as ferroelectricity, magnetism, superconductivity, or multiferroic behavior. Recent achievements in the atomic-scale fabrication of oxide heterostructures by means of pulsed laser deposition (PLD) and molecular beam epitaxy (MBE) made it feasible to combine these intrinsic functionalities with those specific for interfaces and thin films as is known from semiconductor technology. This paves the way not only for tuning the interactions in transition metal oxides to stabilize known phases but also for the creation of novel quantum states, which are not present in the bulk constituents [26]. Such control can be realized by design, the materials choice, applying a gate voltage, or strain. The common scheme thereby is to realize a re-balancing of the interactions of the charge, spin, orbital, or lattice degrees of freedom.

The paradigm for this new class of hybrid materials is the two-dimensional electron system (2DES) which forms at the interface of $\text{LaAlO}_3/\text{SrTiO}_3$ (LAO/STO), although both oxides are band insulators [27]. Intriguingly, the 2DES exists only at a LAO thickness of 4 unit cells (uc) or bigger if the LAO film has been grown on a TiO_2 -terminated STO(001) substrate [28]. Meanwhile, a vast array of intriguing properties has been found for this interface system, among them magnetic Kondo scattering [29], two-dimensional (2D) superconductivity [30], and a large electric-field enabling switching of the interface (super)conductivity by application of suitable gate voltages [28, 31]. More recently, phase separation or even coexistence of magnetism and superconductivity have been discovered at low temperatures [32–35].

The physical origin of the 2DES formation, however, is still debated. The observation that both interface-conductivity as well as ferromagnetism only appear for a critical LAO thickness of 4 unit cells (uc) and beyond [28, 36] has been related to electronic reconstruction. In this scenario electrons are transferred from the surface to the interface in order to minimize the electrostatic energy resulting from the polar discontinuity between LAO and STO [37]. While STO consists of charge neutral SrO and TiO_2 layers, LAO exhibits alternating $(\text{LaO})^+$ and $(\text{AlO}_2)^-$ lattice planes, which act like a series of parallel-plate capacitors [38] resulting in a polarization field across the LAO film. If the potential difference across the LAO gets large enough with increasing thickness, electrons are transferred to the interface to (partially) neutralize the electrostatic gradient. Alternative explanations involve doping by oxygen vacancies and/or cation intermixing (cf. also section 3.3).

The challenge for the notoriously surface-sensitive PES consists in accessing the interface buried below an overlayer of about 2 nm. This became possible only several years ago at 3rd generation synchrotron radiation sources that provide sufficiently high photon fluxes for measurements in the hard x-ray regime with high energy resolution and count rates [39]. Obviously, to gain a microscopic understanding of the origin and nature of the 2DES it is key to know about its vertical extension and the charge carrier concentration. As opposed to most other methods, HAXPES can provide this information non-destructively on as-is samples.

The simple idea is to exploit the angle-dependence of the effective inelastic mean free path

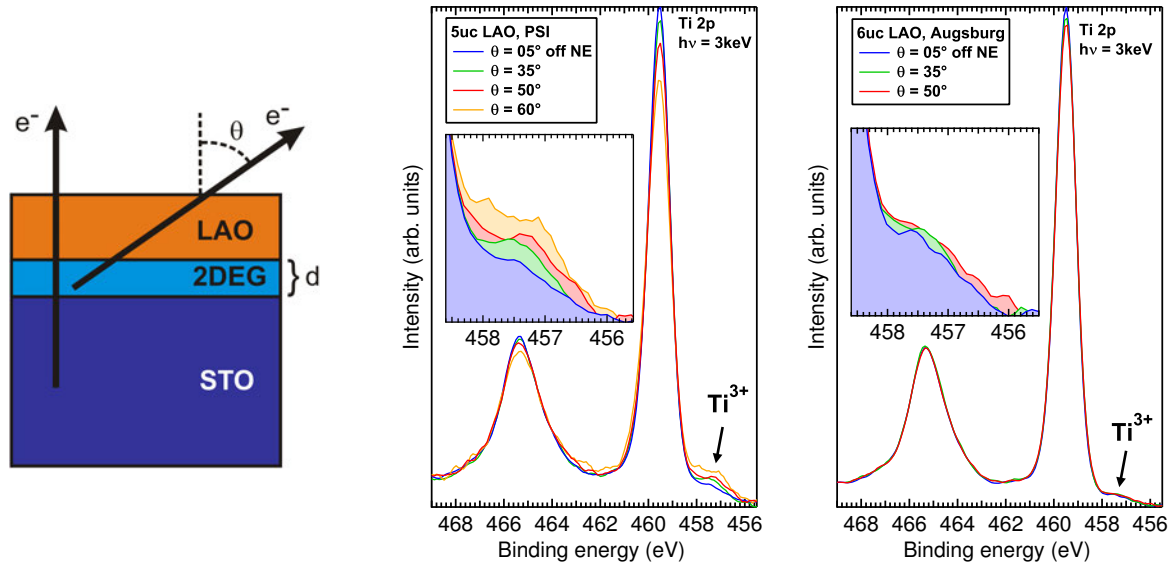


Fig. 7: Left: Sketch of the measuring geometry for angle-dependent HAXPES experiments on a LAO/STO heterostructure with an interface 2DES. Middle and right: Ti 2p spectra of two different LAO/STO heterostructures with varying emission angle θ (from [40]).

$\lambda_{\text{eff}} = \lambda_{\text{INFP}} \cos \theta$ to perform depth profiling, e.g., of the vertical distribution of an element with a certain oxidation state in the geometry as sketched in Fig. 7, left [40]. Figure 7 depicts in the middle and on the right Ti 2p spectra of two different LAO/STO samples with a conducting interface, recorded at a photon energy of 3 keV and with varying detection angle θ relative to the surface normal [40]. The spectra are normalized to integral intensity. The interesting feature is the tiny spectral weight at lower binding energies with respect to the main line, which is shown as close-up in the respective insets.

Due to its chemical shift it can be attributed to the emission from the 2p core level of Ti^{3+} ions, whereas the main line originates from that of Ti^{4+} sites. An additional electron in the d shell results in a more effective screening of the core-potential and hence a shift to lower binding energies. This feature thus provides indirect evidence of the existence of extra electrons in STO in which Ti otherwise is in a 4+ valence state. It is now interesting to realize that in the spectra of Fig. 7 the emission from Ti ions in the oxidation state 3+ increases with larger detection angle, i.e., with smaller information depth and hence higher sensitivity to the interface. This means that the region in STO with extra electrons is indeed confined to the interface and has a vertical extension of the order of the inelastic mean free path of the photoelectrons. Otherwise no angular dependence would be observed.

A more detailed, quantitative analysis of the angle dependence of the ratio of the 2p emission from Ti^{3+} and Ti^{4+} ions, based on a simple model assuming a homogeneous 2DES of thickness d as in Fig. 7, left, allows for an estimate of the sheet carrier density and the thickness of the 2DES. To do so one just has to integrate the contributions of the respective Ti species to the photoemission signal according to their vertical distribution, taking into account the damping factor $e^{-z/\lambda_{\text{eff}}}$ for photoelectrons created at a depth z below the interface [40]. The results are the following: (i) The sheet carrier densities are about one order of magnitude lower than

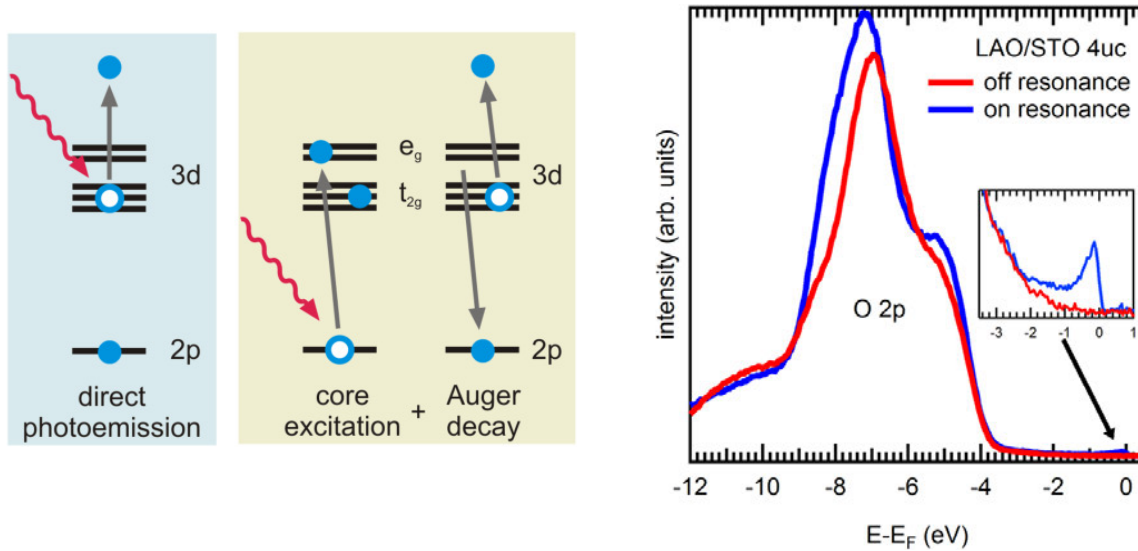


Fig. 8: *Left: Sketch of the direct PES and the Auger-like channel which quantum mechanically interfere in ResPES. Right: Angle-integrated on- and off-resonance spectra of the valence band in LAO/STO. The resonance enhancement in the region of O 2p emission (below ≈ 3.5 eV) is due to O 2p-Ti 3d hybridization.*

expected in an ideal electronic reconstruction scenario as also is inferred from Hall data [28]. (ii) At variance with the latter, already in samples with a non-conducting interface a finite charge carrier concentration is observed by HAXPES. Moreover, the charge carrier concentrations as inferred from the HAXPES data do not exhibit a jump with increasing LAO thickness but rather a continuous increase. (iii) The vertical extension of the 2DES amounts to only a few unit cells at room temperature.

It is difficult to reconcile these results, in particular (i) and (ii), with the standard electronic reconstruction scenario as mechanism for the formation of the 2DES. In the next section, we will see that in view of the findings by resonant soft x-ray PES the ideal electronic reconstruction actually has to be discarded.

3.3 Resonant angle-resolved soft x-ray photoemission: Direct k -space mapping of the electronic structure in an oxide-oxide interface

In the previous section we saw that HAXPES on the Ti 2p core-levels provides indirect evidence for the interface 2DES in LAO/STO. A direct observation of the 3d states contributing to the 2DES is hindered by the low photoionisation cross section at these high photon energies. Even for energies in the soft x-ray regime around 500 eV which would just grant a sufficiently high probing depth to access the buried interface the Ti 3d photoemission signal is too low for measurements to be feasible. However, there is a special technique called resonant PES (ResPES) which allows for a selective enhancement of the photoemission signal from specific orbitals by tuning the photon energy to an appropriate absorption threshold. According to the dipole selection rules, in our case the apt absorption threshold in the soft x-ray regime is the Ti L edge ($2p \rightarrow 3d$ transitions). There, an additional Auger-like channel opens which leads to the same

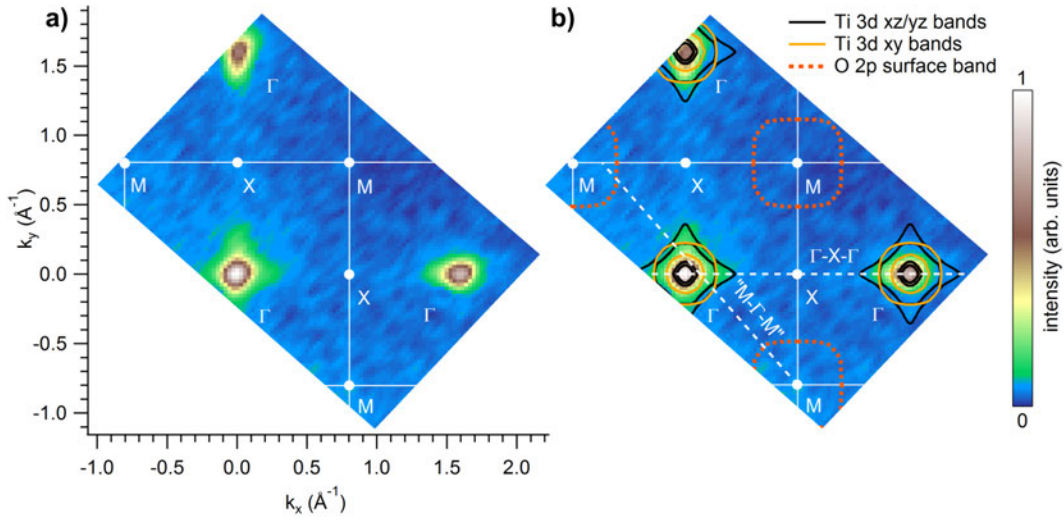


Fig. 9: (a) Fermi surface map recorded at 460.20 eV. (b) Same map as (a) but with the Fermi surface sheets from density-functional calculations overlaid (from [41]).

final state as in the direct PES process (see Fig. 8)

$$2p^6 3d^n \rightarrow 2p^6 3d^{n-1} + \epsilon \quad (\text{direct PES}), \quad (14)$$

$$2p^6 3d^n \rightarrow 2p^5 3d^{n+1} \rightarrow 2p^6 3d^{n-1} + \epsilon \quad (\text{Auger decay}), \quad (15)$$

where ϵ denotes the ejected photoelectron. The probability amplitudes of both channels interfere quantum mechanically and thus give rise to an enhanced $3d$ spectral weight. How effectively the resonant enhancement indeed works can be judged from the comparison of angle-integrated on- and off-resonance spectra in Fig. 8. Off-resonance, no hint to the Ti $3d$ states is discernable at the chemical potential, while on-resonance, a sharp quasiparticle peak is observed.

Since momentum information is still preserved using soft x-rays one now can exploit the resonance enhancement to perform even k -space mapping of the 2DES interface states. By integration of the recorded EDCs for each k point over an interval of 0.3 eV centered around the Fermi energy, one obtains the Fermi surface map in Fig. 9 [41]. One finds an isotropic contribution of high intensity around the Γ points of the Brillouin zone of STO. As is best seen for the lower left Γ point in Fig. 9, the spectral weight also extends towards the X points, forming a flower-like intensity distribution. These observations are consistent with the results of density-functional calculations of the Fermi surface sheets, which are overlaid on top of the PES data in Fig. 9(b) [41].

However, there is also a striking discrepancy: In the calculations, a hole-like Fermi surface is predicted around the M points as marked by the red dashed lines. It originates from O $2p$ states at the valence band maximum of LAO. This simply reflects the standard electronic reconstruction scenario in which the valence band maximum follows the built-in potential across the LAO overlayer towards the Fermi level. At the critical thickness, the valence band crosses the Fermi level at the very surface of the LAO film and gives rise to the hole pockets around M while the released electrons are transferred to the STO conduction band minimum.

The absence of such hole pockets thus leads to the conclusion that the built-in potential is basically screened out in the LAO film. This possibly could be caused by the separation of photogenerated electron-hole pairs in the initial polarization field. However, there are several indications against it. Samples with an insulating interface do charge up in HAXPES which should not happen if there was a significant amount of photogenerated charge carriers. Varying the photon flux by several orders of magnitude does not result in any noticeable changes of the spectra [42]. In a related heterostructure with a polar/non-polar interface a built-in potential has been observed by x-ray photoelectron spectroscopy [43].

Alternatively, the experimental observations can be reconciled by proposals, based mainly on density-functional calculations, that O vacancies at the very surface of the LAO film can serve as a charge reservoir for the electronic reconstruction [44–47]. Such O vacancies induce unoccupied, localized in-gap states. The two released electrons per vacancy are transferred to the interface and thereby the polarization field is efficiently reduced and finally screened out almost completely. Note that we recover the critical thickness in this picture since, with increasing thickness of the LAO film considered as a parallel-plate capacitor, at some stage the electrostatic energy gain for discharging due to the transfer of two electrons per oxygen vacancy outweighs its formation energy.

4 Outlook

In this brief introduction into photoelectron spectroscopy of complex quantum materials only a very small portion of the entire field could be covered. And even there only a few essential aspects could be touched upon. Nevertheless, it should have become clear that photoelectron spectroscopy in all its variants is a very versatile tool to study basically all kind of complex materials exhibiting interesting many-body phenomena. Although photoelectron spectroscopy is a mature, well-established technique the frontiers of its capabilities have been pushed back by technological progress regarding light sources, electron analyzers, and detectors during the last twenty years and this evolution still continues. Current developments are directed towards a further improvement of fast detectors with parallel data acquisition, high brilliance tunable light sources (also with well-defined time structure for time-resolved experiments), electron analyzers with respect to energy and momentum resolution, and spin detection.

Acknowledgments

Part of the work described in this contribution is the result of the author's fruitful collaborations with many researchers. Their names may be found in the respective original papers listed below. Financial support by BMBF (05 KS7WW3, 05 K10WW1) and DFG (CL124/6-1, CL124/6-2, FOR 1162, FOR 1346) is gratefully acknowledged.

References

- [1] M. Cardona and L. Ley (eds.): *Photoemission in solids I* (Springer, Berlin, 1978)
- [2] B. Feuerbacher, B. Fitton, and R.F. Willis (eds.):
Photoemission and the electronic properties of surfaces (Wiley, New York, 1978)
- [3] S.D. Kevan (Ed.): *Angle resolved photoemission – theory and current applications*,
Studies in surface science and catalysis, Vol. 74 (Elsevier, Amsterdam, 1992)
- [4] S. Hüfner: *Photoelectron spectroscopy. Principles and applications*
(Springer, Berlin, 2003)
- [5] W. Schattke and M.A. van Hove (Eds.): *Solid-state photoemission and related methods:
theory and experiment* (Wiley-VCH, Weinheim, 2003)
- [6] L. Hedin and S. Lundqvist: *Effects of electron-electron and electron-phonon interactions
on the one-electron states of solids*, in: H. Ehrenreich, D. Turnbull (eds.):
Solid State Physics, Vol. 23 (Academic Press, New York, 1969)
- [7] C.O. Almbladh and L. Hedin in E.E. Koch (Ed.) *Handbook on synchrotron radiation* Vol. 1
(North-Holland, Amsterdam, 1983), p. 607
- [8] A. Damascelli, Z. Hussain, and Z.-X. Shen, *Rev. Mod. Phys.* **75**, 473 (2003)
- [9] F. Reinert and S. Hüfner, *New J. Phys.* **7**, 97 (2005)
- [10] R. Claessen, J. Schäfer, and M. Sing: *Photoemission on quasi-one-dimensional solids:
Peierls, Luttinger & Co.* in: *Very High Resolution Photoelectron Spectroscopy*, ed. by
S. Hüfner, *Lecture Notes in Physics*, Vol. 715 (Springer, Berlin, 2007)
- [11] S. Suga and A. Sekiyama (eds.): *Photoelectron Spectroscopy: Bulk and Surface Electronic
Structures*, Springer Series in Optical Sciences, Vol. 176 (Springer, Berlin, 2014)
- [12] A. Avella and F. Mancini (eds.): *Strongly Correlated Systems: Experimental Techniques*,
Springer Series in Solid-State Sciences, Vol. 180 (Springer, Berlin, 2014)
- [13] G.A. Sawatzky, *Nature* **342**, 480 (1989)
- [14] L. Hedin and J.D. Lee, *J. Electron Spectrosc. Relat. Phenom.* **124**, 289 (2002)
- [15] R.J. Beynon and J.A. Wilson, *J. Phys.: Condens. Matter* **5**, 1983 (1993)
- [16] A. Seidel, C.A. Marianetti, F. C. Chou, G. Ceder, and P.A. Lee,
Phys. Rev. B **67**, 020405(R) (2003)
- [17] M. Shaz, S. van Smaalen, L. Palatinus, M. Hoinkis, M. Klemm, S. Horn, and R. Claessen,
Phys. Rev. B **71**, 100405(R) (2005)

- [18] R. Rückamp, J. Baier, M. Kriener, M.W. Haverkort, T. Lorenz, G.S. Uhrig, L. Jongen, A. Möller, G. Meyer, and M. Grüninger, *Phys. Rev. Lett.* **95**, 097203 (2005)
- [19] H. Schäfer, F. Wartenpfehl, and E. Weise, *Z. Anorg. Allg. Chem.* **295**, 268 (1958)
- [20] M. Sing, S. Glawion, M. Schlachter, M.R. Scholz, K. Goß, J. Heidler, G. Berner, and R. Claessen, *Phys. Rev. Lett.* **106**, 056403 (2011)
- [21] S. Yamanaka, T. Yasunaga, K. Yamaguchi, and M. Tagawa, *J. Mater. Chem.* **19**, 2573 (2009)
- [22] Y.-Z. Zhang, K. Foyevtsova, H.O. Jeschke, M.U. Schmidt, and R. Valentí, *Phys. Rev. Lett.* **104**, 146402 (2010)
- [23] J.S. Lee, M.W. Kim, and T.W. Noh, *New J. Phys.* **7**, 147 (2005)
- [24] M. Hoinkis, M. Sing, J. Schäfer, M. Klemm, S. Horn, H. Benthien, E. Jeckelmann, T. Saha-Dasgupta, L. Pisani, R. Valentí, and R. Claessen, *Phys. Rev. B* **72**, 125127 (2005)
- [25] C.A. Kuntscher, S. Frank, A. Pashkin, M. Hoinkis, M. Klemm, M. Sing, S. Horn, and R. Claessen, *Phys. Rev. B* **74**, 184402 (2006)
- [26] H.Y. Hwang, Y. Iwasa, M. Kawasaki, B. Keimer, N. Nagaosa, and Y. Tokura, *Nature Mater.* **11**, 103 (2012)
- [27] A. Ohtomo and H.Y. Hwang, *Nature* **427**, 423 (2004)
- [28] S. Thiel, G. Hammerl, A. Schmehl, C.W. Schneider, and J. Mannhart, *Science* **313**, 1942 (2006)
- [29] A. Brinkman, M. Huijben, M. van Zalk, J. Huijben, U. Zeitler, J.C. Maan, W.G. van der Wiel, G. Rijnders, D.H.A. Blank, and H. Hilgenkamp, *Nature Mater.* **6**, 493 (2007)
- [30] N. Reyren, S. Thiel, A.D-Cavaglia, L.F. Kourkoutis, G. Hammerl, C. Richter, C.W. Schneider, T. Kopp, A.-S. Ruetschi, D. Jaccard, M. Gabay, D.A. Müller, J.-M. Triscone, and J. Mannhart, *Science* **317**, 1196 (2007)
- [31] A.D. Cavaglia, S. Gariglio, N. Reyren, D. Jaccard, T. Schneider, M. Gabay, S. Thiel, G. Hammerl, J. Mannhart, and J.-M. Triscone, *Nature* **456**, 624 (2008)
- [32] Ariando, X. Wang, G. Baskaran, Z.Q. Liu, J. Huijben, J.B. Yi, A. Annadi, A.R. Barman, A. Rusydi, S. Dhar, Y.P. Feng, J. Ding, H. Hilgenkamp, and T. Venkatesan, *Nature Commun.* **2**, 188 (2011)
- [33] D.A. Dikin, M. Mehta, C.W. Bark, C.M. Folkman, C.B. Eom, and V. Chandrasekhar, *Phys. Rev. Lett.* **107**, 056802 (2011)
- [34] L. Li, C. Richter, J. Mannhart, and R. Ashoori, *Nat. Phys.* **7**, 762 (2011)

- [35] J.A. Bert, B. Kalisky, C. Bell, M. Kim, Y. Hikita, H.Y. Hwang, and K.A. Moler, *Nature Phys.* **7**, 767 (2011)
- [36] B. Kalisky, J.A. Bert, B.B. Klopfer, C. Bell, H.K. Sato, M. Hosoda, Y. Hikita, H.Y. Hwang, and K.A. Moler, *Nature Commun.* **3**, 922 (2012)
- [37] N. Nakagawa, H.Y. Hwang, and D.A. Müller, *Nature Mater.* **5**, 204 (2006)
- [38] C. Noguera, *J. Phys.: Condens. Matter* **12**, R367 (2000)
- [39] K. Kobayashi, *Nucl. Instrum. Methods Phys. Res. A* **601**, 32 (2009)
- [40] M. Sing, G. Berner, K. Goß, A. Müller, A. Ruff, A. Wetscherek, S. Thiel, J. Mannhart, S.A. Pauli, C.W. Schneider, P.R. Willmott, M. Gorgoi, F. Schäfers, and R. Claessen, *Phys. Rev. Lett.* **102**, 176805 (2009)
- [41] G. Berner, M. Sing, H. Fujiwara, A. Yasui, Y. Saitoh, A. Yamasaki, Y. Nishitani, A. Sekiyama, N. Pavlenko, T. Kopp, C. Richter, J. Mannhart, S. Suga, and R. Claessen, *Phys. Rev. Lett.* **110**, 247601 (2013)
- [42] G. Berner, A. Müller, F. Pfaff, J. Walde, C. Richter, J. Mannhart, S. Thiess, A. Gloskovskii, W. Drube, M. Sing, and R. Claessen, *Phys. Rev. B* **88**, 115111 (2013)
- [43] S.A. Chambers, L. Qiao, T.C. Droubay, T.C. Kaspar, B.W. Arey, and P.V. Sushko, *Phys. Rev. Lett.* **107**, 206802 (2011)
- [44] Z. Zhong, P.X. Xu, and P.J. Kelly, *Phys. Rev. B* **82**, 165127 (2010)
- [45] N.C. Bristowe, P.B. Littlewood, and E. Artacho, *Phys. Rev. B* **83**, 205405 (2011)
- [46] Y. Li, S.N. Phattalung, S. Limpijumnong, J. Kim, and J. Yu, *Phys. Rev. B* **84**, 245307 (2011)
- [47] N. Pavlenko, T. Kopp, E.Y. Tsymbal, J. Mannhart, and G.A. Sawatzky, *Phys. Rev. B* **86**, 064431 (2012)